A surface electrode point Paul trap

Tony Hyun Kim,[1,*] Peter F. Herskind,[1] Taehyun Kim,[2] Jungsang Kim,[2] and Isaac L. Chuang[1]

[1] *Center for Ultracold Atoms, Department of Physics, Massachusetts Institute of Technology 77 Massachusetts Avenue, Cambridge, MA 02139*

[2] *Department of Electrical and Computer Engineering, Duke University Durham, NC 27708*

(Dated: July 23, 2010)

We present a model as well as experimental results for a surface electrode radio-frequency Paul trap that has a circular electrode geometry well-suited for trapping of single ions and two-dimensional planar ion crystals. The trap design is compatible with microfabrication and offers a simple method by which the height of the trapped ions above the surface may be changed *in situ*. We demonstrate trapping of single $^{88}Sr^+$ ions over an ion height range of 200–1000μm for several hours under Doppler laser cooling, and use these to characterize the trap, finding good agreement with our model.

I. INTRODUCTION

Radiofrequency (rf) traps have been applied extensively in a large variety of scientific studies over the past six decades. Originating from mass spectrometry [1], they have then been applied in fields such as metrology [2], quantum information science [3, 4] and cold molecular physics [5, 6], to mention but a few.

Traditionally, such devices have been rather bulky, three-dimensional structures that required precise machining and careful assembly. Recently, however, the four-rod linear Paul trap (see Fig. 1a) has been transformed into a two-dimensional structure, with all electrodes in a single plane above which ions can be trapped [7]. This new class of so-called surface traps offer a tremendous advantage over their predecessors in that electrodes can be defined lithographically with extremely high precision and that construction can leverage the techniques of microfabrication, with the possibility of incorporating the technology of CMOS for integrated control hardware [8, 9]. These aspects are particularly attractive to applications in quantum information processing where limitations are currently, by a large degree, pertaining to the scalability of devices for trapping as well as certain elements of infrastructure such as optics, laser light delivery, and control electronics.

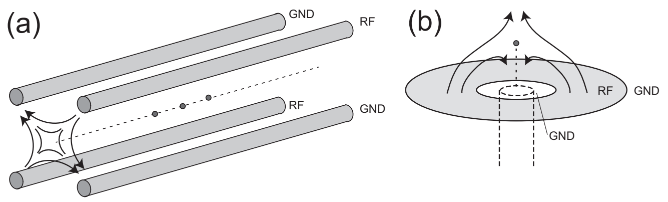

FIG. 1. Comparison of the traditional four-rod linear Paul trap (a) to the Point Paul trap (b). The latter achieves quadrupole ion confinement through rf on a single, ring-shaped electrode. Dashed lines suggest how cylindrical elements – such as optical fibers – may be introduced to the point Paul geometry.

In this paper we study a novel type of rf surface trap with a high degree of symmetry in its electrode geometry. The generic geometry of this trap, which we shall refer to as the point Paul trap, is shown in Fig. 1b, and may consist of any number of concentric electrodes of arbitrary widths to which different voltages can be applied. This design is strongly inspired by work on planar Penning traps [10], where a similar geometry was used to create a static electric quadrupole field that, when combined with a strong homogeneous magnetic field, gave rise to a confining potential above the surface of the electrodes. The point Paul trap also bears close resemblance to the rf ring- and the rf hole-traps [11]; however differs in that the ion is trapped above the surface of the electrodes as opposed to in-between, which makes this geometry better suited for microfabrication.

A consequence of the azimuthal symmetry of the electrodes is that the rf-field exhibits a nodal point rather that a nodal line as in the linear Paul trap and that the confining fields originate exclusively from the rf-potential, rendering the addition of dc-potentials nonessential for anything but the compensation of stray charges on the trap. This makes the point Paul trap well-suited for confinement of single ions, which may then reside at the rf-nodal point where the amplitude of the rapidly oscillating rf-field vanishes.

The ability to fabricate these traps in a scalable fashion makes them attractive for realizing large arrays of single ions in independent traps that may be utilized for a quantum processor, provided the individual ions can be interconnected, e.g., through optical fibers [12, 13]. On this aspect, the axial symmetry of the trap lends itself well to integration of such fibers and potentially other optical elements that also possess axial symmetry. The fiber, for instance, may be introduced through the electrodes directly beneath the ions with minimal perturbation of the trapping fields.

Another possible application of this trap is in the field of quantum simulation. While classical computers are unable to efficiently simulate coupled spin systems, such simulations may be implemented using a quantum mechanical system of effective spins, such as

* kimt@mit.edu

a two-dimensional lattice of interacting ions. The resulting potential of the point Paul trap provides ion crystals with exactly the requisite two-dimensional planar structure. As such, the system could be used to simulate e.g. a frustrated spin system [14], as was demonstrated recently[15].

We also find that our trap design is ideally suited for realizing a scheme by which the height of a single trapped ion above the trap surface is varied *in-situ*. This capability may prove extremely useful in the search for the origin of anomalous heating in ion traps – a problem currently impeding the advancement of quantum computation with trapped ions [16, 17]. It also provides a general technique by which oven contamination of the trap can be minimized by loading further away from the trap surface, and subsequently bringing the ion to the desired trap height.

This paper is organized as follows: in Section II we present a model for the planar point Paul trap, derive analytic expressions for the relevant trapping parameters, present full numerical results of trap optimization, and consider a scheme for the variation of the ion height above the trap surface. In Section III we describe our experimental setup used for the verification of the model; and in Section IV we present experimental results for trapping of single and few ions in a printed circuit board (PCB) implementation of the point Paul trap.

II. POINT PAUL TRAP MODEL

We proceed with a general treatment applicable to an arbitrary number of circular electrodes, and then focus on a particular geometry that we will study experimentally later in Sections III and IV. At the end of this section we also describe a scheme for variation of the ion height above the trap surface.

A. Potential from annular planar electrodes

We begin with the general solution to the Laplace equation in charge-free space and express this in cylindrical coordinates for $z \geq 0$, yielding [18]

$$\Phi(z,\rho,\phi) = \sum_{m=0}^{\infty} \int_0^{\infty} J_m(k\rho) e^{-kz} \times \left[\mathcal{A}_m(k)\cos(m\phi) + \mathcal{B}_m(k)\sin(m\phi)\right] dk. \tag{1}$$

where $J_m(k\rho)$ are the usual Bessel functions and $\mathcal{A}_m(k)$ and $\mathcal{B}_m(k)$ are coefficients to be determined based on the boundary conditions of the problem. Based on the azimuthal symmetry of Fig. 2, Eq. (1) further simplifies to [18]

$$\Phi(z,\rho) = \int_0^{\infty} J_0(k\rho) e^{-kz} \mathcal{A}_0(k) dk. \tag{2}$$

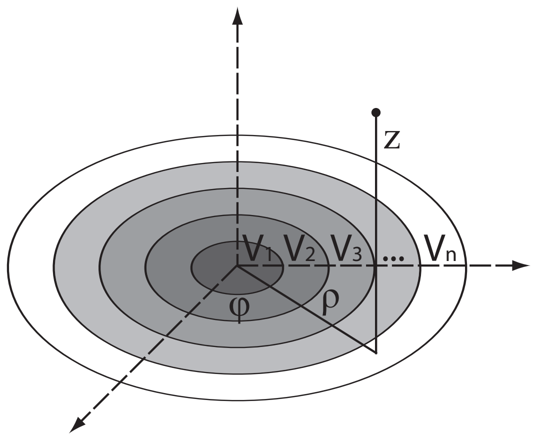

FIG. 2. The generic layout of the point Paul trap, which consists of concentric annular electrodes with arbitrary widths, as illustrated above in a cylindrical coordinate system.

In turn, $\mathcal{A}_0$ can be expressed as $\mathcal{A}_0(k) = \sum_i^n A_i(k)$, where

$$A_i(k) = k \int_{\alpha_i}^{\beta_i} \rho J_0(k\rho) V_i(\rho) d\rho. \tag{3}$$

All information about the electrode geometry is now included in the $\mathcal{A}_0$ coefficient, which we have in turn written as a sum of n sub-coefficients, each accounting for the effect of a single annular electrode i with inner radius α_i, outer radius β_i and a voltage V_i, which we shall assume is constant across the electrode. The integral of Eq. (3) can be evaluated using the identity for the Bessel functions $\int_0^u dv J_0(v) = uJ_1(u)$ to give

$$A_i(k) = V_i \left[\beta_i J_1(k\beta_i) - \alpha_i J_1(k\alpha_i)\right]. \tag{4}$$

This completes the general treatment of the problem: The electric potential above a surface at $z = 0$ with n concentric circular electrodes, each with independent voltages V_i and inner and outer radii of α_i and β_i respectively, is given by Eq. (2) with $\mathcal{A}_0(k) = \sum_i^n A_i(k)$, where the A_i coefficients are given by Eq. (4).

B. The three-electrode point Paul trap

While static potentials alone may provide confinement in one or two dimensions, Earnshaw's theorem dictates that this is accompanied by a defocusing effect in the orthogonal dimensions. In the work of Ref. [10], three-dimensional confinement was achieved via the addition of a static magnetic field to realize a planar Penning trap. Here, we use a time-varying rf field to achieve charge confinement, as a planar Paul trap. For the remainder of this work, we consider the simple geometry of only three electrodes defined by the following boundary conditions:

$$\Phi(z=0,\rho)=\begin{cases}0 & \text{for } 0<\rho<a,\\ V_{\mathrm{rf}}\cos(\Omega_{\mathrm{rf}}t) & \text{for } a\le\rho\le b,\\ 0 & \text{for } b<\rho<\infty,\end{cases} \tag{5}$$

where V_{rf} is the amplitude of the applied voltage and Ω_{rf} is the frequency. The resulting potential then reads

$$\Phi(z,\rho,t)=V_{\mathrm{rf}}\cos(\Omega_{\mathrm{rf}}t)\kappa(z,\rho), \tag{6}$$

where

$$\kappa(z,\rho)=\int_0^\infty\left[bJ_1(kb)-aJ_1(ka)\right]e^{-kz}J_0(k\rho)dk. \tag{7}$$

In general, Eq. (7) has to be solved numerically. However, for the case of $\rho=0$ the problem simplifies significantly and an analytic solution can be obtained. From the symmetry of the problem we can infer that if a non-trivial field zero ($\vec{E}=0$) exists for $z>0$, it will be located on the axis defined by $\rho=0$ and hence this scenario is worthy of attention.

The on-axis potential is easily integrated to yield:

$$\kappa(z,0)=\frac{1}{\sqrt{1+(\frac{a}{z})^2}}-\frac{1}{\sqrt{1+(\frac{b}{z})^2}}. \tag{8}$$

Asserting that this potential provides for an electric field null at $z=z_0>0$, we expand $\Phi(z,t)$ around this point and use the resulting expansion to find the equation of motion for a particle of mass M and charge Q along the z-axis:

$$\begin{aligned}\ddot{z}(t)&=-\frac{Q}{M}\frac{\partial\Phi(z,t)}{\partial z}\\ &\simeq-\frac{QV_{\mathrm{rf}}}{M}\cos(\Omega_{\mathrm{rf}}t)\times\left[f(a,b)(z-z_0)+O(z-z_0)^2\right].\end{aligned} \tag{9}$$

Provided $|z-z_0|\ll z_0$, which is a reasonable assumption for a trapped ion, terms of second and higher order can be neglected, and the equation of motion takes the form of the well-known Mathieu equation. With proper rescaling of variables, Eq. (9) can be cast into the standard Mathieu form [19]:

$$\ddot{\tilde{z}}(\tau)+2q\cos(2\tau)\tilde{z}(\tau)=0, \tag{10}$$

where we have substituted $\tilde{z}=z-z_0$ and $\tau=\Omega_{\mathrm{rf}}t/2$, and the Mathieu q-parameter has been defined as

$$q=\frac{2QV_{\mathrm{rf}}}{M\Omega_{\mathrm{rf}}^2}f(a,b). \tag{11}$$

Here, everything related to the trap geometry is collected into a single function $f(a,b)$ of unit $[\text{length}]^{-2}$ given by

$$f(a,b)=\sqrt{\frac{9(b^{\frac{2}{3}}-a^{\frac{2}{3}})^2(b^{\frac{2}{3}}+a^{\frac{2}{3}})^6}{b^{\frac{4}{3}}a^{\frac{4}{3}}(b^{\frac{4}{3}}+b^{\frac{2}{3}}a^{\frac{2}{3}}+a^{\frac{4}{3}})^5}}. \tag{12}$$

Note that in this treatment a denotes the inner radius of the rf electrode and not the Mathieu a-parameter, commonly used in the literature on Paul traps. The Mathieu a-parameter, which corresponds to the inclusion of a dc-potential in the equation of motion (Eq. 9), is rendered superfluous in the point Paul trap as full three-dimensional confinement is achieved in this geometry by the rf-field alone.

When the trap is operated such that $|q|\ll 1$, the equation of motion can be readily solved to yield

$$\tilde{z}(t)=\sigma_0\left[1-\frac{q}{2}\cos(\Omega_{\mathrm{rf}}t)\right]\cos(\omega_z t). \tag{13}$$

This is the usual result, familiar also from the four-rod linear Paul trap, where the motion is comprised of two distinct types of motion: a slow, so-called *secular*, motion with an amplitude σ_0 at a frequency

$$\omega_z=\frac{q}{2\sqrt{2}}\Omega_{\mathrm{rf}}=\frac{QV_{\mathrm{rf}}}{\sqrt{2}M\Omega_{\mathrm{rf}}}f(a,b) \tag{14}$$

and a superimposed, fast *micromotion*, with a lower amplitude of $\frac{1}{2}q\sigma_0$ and at sideband frequencies of the rf drive Ω_{rf}. Neglecting the micromotion – a reasonable approximation for $|q|\ll 1$ – we can define an approximate harmonic potential that describes the ion motion near the quadrupole zero by the following

$$\Psi(z)=\frac{1}{2}M\omega_z^2(z-z_0)^2=\frac{Q^2V_{\mathrm{rf}}^2}{4M\Omega_{\mathrm{rf}}^2}f^2(a,b)(z-z_0)^2, \tag{15}$$

thereby showing the charge-confining capabilities of the three-electrode point Paul trap, provided that $f^2>0$.

C. Trap optimization and results

While the harmonic potential of Eq. (15) provides an intuitive connection to the physical, time-averaged motion of the trapped ion in the vicinity of the rf node, it does not reveal any information about the dynamics where the inequality $|z-z_0|\ll z_0$ is not satisfied. For instance, in a real device there is necessarily a finite trapping volume and trap depth. These quantities originate from the shape of the pseudopotential significantly beyond the harmonic region. In the limit $q\ll 1$, the effective potential energy beyond the harmonic regime – commonly referred to as the *pseudopotential* – may be expressed directly through the gradient of the electric potential, here written in terms of κ, as [20–22]

$$\Psi(z,\rho)=\frac{Q^2V_{\mathrm{rf}}^2}{4M\Omega_{\mathrm{rf}}^2}\left|\nabla\kappa(z,\rho)\right|^2. \tag{16}$$

The solid line in Fig. 3 shows the pseudopotential for the planar point Paul trap. Superimposed is the harmonic approximation (dashed line). Inserting the expression for κ from Eq. (7) into the expression for the pseudopotential

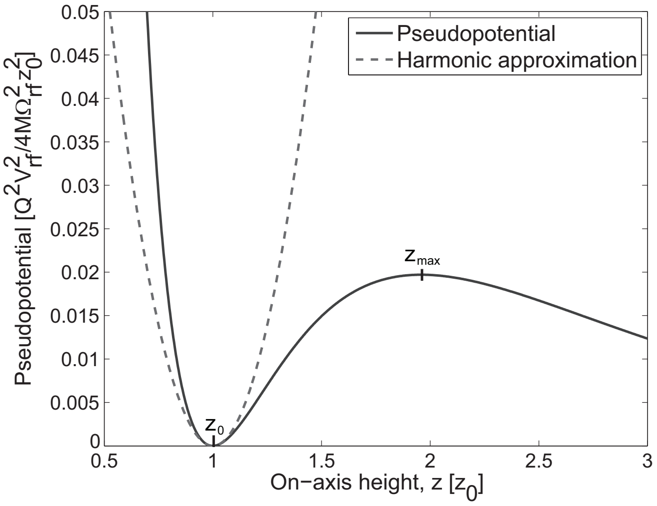

FIG. 3. The harmonic potential approximation (Eq. 15; dashed line) for the point Paul trap is shown on top of the pseudopotential (Eq. 16; solid line). The latter identifies the trap turn-around point z_{max} in addition to the trap location z_0. Trap geometry (a, b) is chosen as in Table I.

(Eq. 16) yields two physically meaningful extrema,

$$z_0 = \sqrt{\frac{b^{4/3}a^{4/3}}{b^{2/3} + a^{2/3}}} \tag{17}$$

and

$$z_{\mathrm{max}} = \sqrt{\frac{b^{6/5} - a^{6/5}}{a^{-4/5} - b^{-4/5}}}. \tag{18}$$

Here, z_0 is the coordinate of the pseudopotential minimum, and z_{max} denotes the turning-point of the confining pseudopotential. The difference $z_{\mathrm{max}} - z_0$ can be taken as a linear measure of the effective trap volume. Furthermore, the corresponding trap depth can now be defined as $D = \Psi(z_{\mathrm{max}}) - \Psi(z_0)$. Using Eq. (17) and Eq. (18), one finds that the trap depth is positive for all values of $b > a > 0$, and is equivalent to:

$$D = \frac{Q^2 V_{\mathrm{rf}}^2}{4M\Omega_{\mathrm{rf}}^2} \left[a^2(a^2 + z_{\mathrm{max}}^2)^{-\frac{3}{2}} - b^2(b^2 + z_{\mathrm{max}}^2)^{-\frac{3}{2}} \right]^2. \tag{19}$$

The trap depth is a reasonable quantity to be optimized in the design of the point Paul trap. However, unconstrained optimization of Eq. (19) over (a, b) will influence not only the trap depth but also the trap height z_0 above the surface through Eq. (17). Often in experiments, the trap height is a parameter of importance and so a more reasonable strategy is to optimize the trap depth for a fixed value of z_0. This can in principle be done analytically; however, the results are more useful in their numerical form. Table I summarizes the results of this optimization. For the purpose of comparison with the four-rod linear Paul trap we have defined

$$q_{\mathrm{4rod}} \equiv \frac{2QV_{\mathrm{rf}}}{M\Omega_{\mathrm{rf}}^2 z_0^2} \quad \text{and} \quad D_{\mathrm{4rod}} \equiv \frac{Q^2 V_{\mathrm{rf}}^2}{4M\Omega_{\mathrm{rf}}^2 z_0^2}, \tag{20}$$

which corresponds to the q-parameter and the trap depth, respectively, for the three-dimensional four-rod Paul trap with an ion-electrode distance of z_0.

TABLE I. Results of numerical optimization of the trap depth for a fixed trap height z_0. The choice of units allows for direct comparison with the three-dimensional linear Paul trap.

$a\,[z_0]$	$b\,[z_0]$	$z_{\mathrm{max}}\,[z_0]$	$q\,[q_{\mathrm{4rod}}]$	$D\,[D_{\mathrm{4rod}}]$
0.651679	3.57668	1.957965	0.471565	0.019703

From the optimization results of Table I, it is seen that the q-parameter of the point Paul trap is roughly a factor $\frac{1}{2}$ of the four-rod linear Paul trap while the trap depth is about a factor $\frac{1}{50}$. By comparison, the surface electrode linear Paul trap design that has recently attracted much attention in the context of quantum computing [23, 24] has q-parameter and a trap depth that are approximately a factor $\frac{1}{2\sqrt{3}}$ and $\frac{1}{72}$, respectively, of the four-rod linear Paul trap [7].

D. 3D potential of the point Paul trap

To extract information about the three-dimensional shape of the pseudopotential, we insert the full expression of Eq. (7) into Eq. (16) and integrate numerically at discrete values of ρ and z. This yields a contour plot as shown in Fig. 4, where the trap dimensions are chosen according to Table I for a trap height of $z_0 = 1$ mm. It is seen that the confinement is tighter along the axial direction of the trap than along the radial direction. Also shown (see insert) is the isosurface corresponding to the edge of the trap.

A unique feature of this trap design is that confinement is achieved in three dimensions using only an rf-field as opposed to the linear trap designs that also require static dc-potentials along the axis defined by the nodal line of the rf quadrupole field. One consequence of this is that, similar to the four-rod linear Paul trap but in contrast to the linear surface electrode Paul trap, the point Paul trap is naturally compensated and dc-potentials are in principle not required for stable trapping.

Another implication of achieving three-dimensional confinement with a single rf-field is that the ratio of the axial and radial secular frequencies is fixed by the geometry of the trap. From quadratic fits to the central harmonic region of Fig. 4, the ratio of the radial to the axial trap frequency is found to be $\frac{\omega_\rho}{\omega_z} \simeq 0.50$.

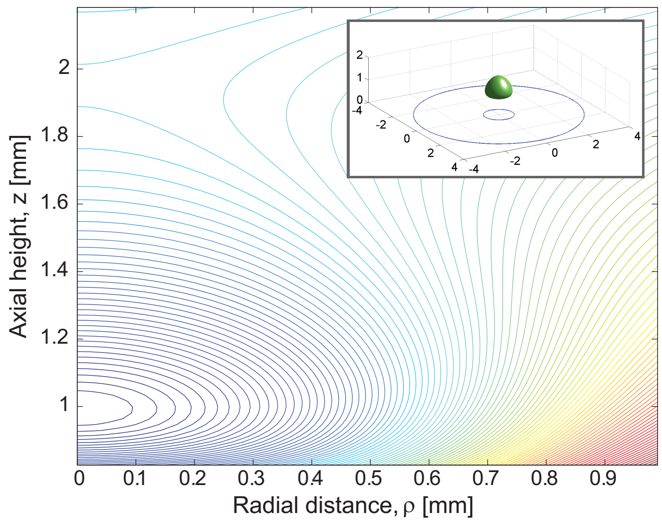

FIG. 4. (Color online) A contour plot for the pseudopotential (Eq. (16)) of a $z_0 = 1$mm trap, using the optimal geometry of Tabe I. Insert shows the trap isosurface in relation to outlines of the rf ring electrode (units in z_0).

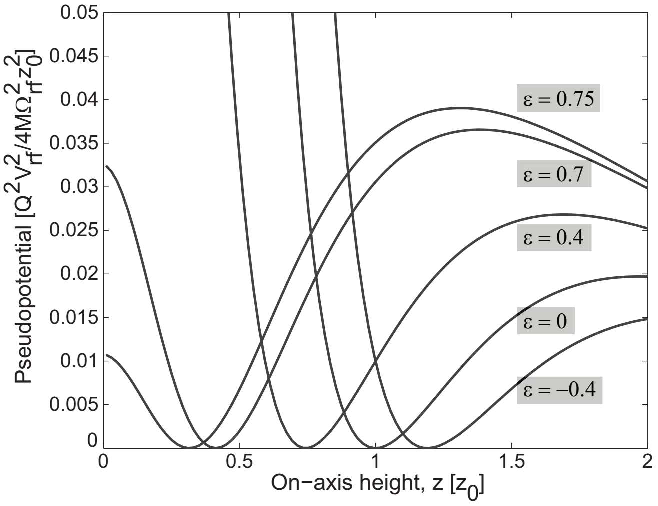

FIG. 5. Variation in the on-axis pseudopotential Ψ with the addition of secondary rf at various values of ϵ. The trap dimensions a and b are as found in Table I.

E. Scheme for variation of the nodal point of the rf-field

We mentioned previously that the ion height above the trap surface is often a parameter of interest and designs are generally optimized with some focus on this parameter. Controlling the ion height *in-situ* is a desirable capability for a variety of experimental applications. To mention a few examples, in experiments incorporating optical cavities, careful alignment of the cavity with respect to the ion is necessary to achieve the highest possible coupling between the ion and the cavity mode [25–28]; and in the study on anomalous heating in ion traps the ion height is a key parameter, with the scaling of the heating rate currently believed to follow a z_0^{-4} trend [16]. The ion position may be adjusted via the addition of dc-potentials; however, unless the rf quadrupole potential is adjusted accordingly, the ion location will not coincide with the zero of the rf field and as a result its motion will be driven by the rapidly changing rf-fields, resulting in broadening of the atomic transitions [29]. It is possible to align the trap relative to external objects such as mirrors by physically moving the trap [25, 27, 28]; however, recently a method for translating the node of the rf quadrupole field has been developed and used both in four-rod Paul traps [30] and in planar surface traps [31, 32] to shift the ions without introducing excess micromotion.

The basic principle of this method is to apply different amplitudes of rf-potential on individual electrodes, thus causing a shift of the rf field node relative to those electrodes. Implementation of this technique is particularly simple in our geometry where it is achieved by adding an rf-field to the central, previously grounded, electrode. The resulting boundary conditions for the electric potential then becomes

$$\Phi(\rho,0) = \begin{cases} \epsilon V_{\rm rf}\cos(\Omega_{\rm rf}t+\theta) & \text{for } 0<\rho<a, \\ V_{\rm rf}\cos(\Omega_{\rm rf}t) & \text{for } a\le\rho\le b, \\ 0 & \text{for } b<\rho<\infty, \end{cases} \tag{21}$$

where ϵ and θ accounts for the amplitude and phase difference between the inner and the outer rf-electrodes.

As before, we again solve the potential for the boundary conditions of Eq. (21), but for the case of either in-phase ($\theta = 0$) or out-of-phase ($\theta = \pi$) drives. The scenario where the two electrodes are related by some other relative phase should be avoided, as it will result in excess micromotion, analogously to the case of the four-rod linear Paul trap [29]. Absorbing the phase into the sign of ϵ, the spatial part of the resulting potential reads

$$\kappa(z,\rho) = \int_0^\infty dk e^{-kz} J_0(k\rho) \times \left[bJ_1(kb) - (1-\epsilon)aJ_1(ka)\right]. \tag{22}$$

We again focus on the case of $\rho = 0$ to find an analytic expression for $\kappa(z,0)$:

$$\kappa(z,0) = \frac{1}{\sqrt{1+(\frac{a}{z})^2}} - \frac{1}{\sqrt{1+(\frac{b}{z})^2}} + \epsilon\left(1-\frac{1}{\sqrt{1+(\frac{a}{z})^2}}\right), \tag{23}$$

where $\epsilon > 0$ and $\epsilon < 0$ correspond to the in-phase and out-of-phase drives, respectively.

Inserting the expression for $\kappa(z)$ into Eq. (16) and using the geometry of Table (I) we may plot the pseudopotential for various values of ϵ. Figure 5 shows such example plots for various values of ϵ. It is seen that the in-phase drive ($\epsilon > 0$) lowers the trap height z_0, while the out-of-phase drive ($\epsilon < 0$) increases the height.

The new trap location and turning point can be found analytically as in Section II C, yielding:

$$z_0'(\epsilon) = \sqrt{\frac{b^2 a^{4/3}(1-\epsilon)^{2/3} - a^2 b^{4/3}}{b^{4/3} - a^{4/3}(1-\epsilon)^{2/3}}} \tag{24}$$

and

$$z_{\max}'(\epsilon) = \sqrt{\frac{b^2 a^{4/5}(1-\epsilon)^{2/5} - a^2 b^{4/5}}{b^{4/5} - a^{4/5}(1-\epsilon)^{2/5}}} \tag{25}$$

We also find an expression for the q-parameter, which is derived analogously to Eq. (11) using (23):

$$q'(\epsilon) = \frac{2QV_{\rm rf}}{M\Omega_{\rm rf}^2}\left[\frac{3a^2 z_0'(1-\epsilon)}{(a^2+z_0'^2)^{5/2}} - \frac{3b^2 z_0'}{(b^2+z_0'^2)^{5/2}}\right]. \tag{26}$$

In addition to the ion height variation, the presence of a second rf modifies the overall shape of the pseudopotential and hence also the effective trap depth, as evidenced already in Fig. 5. Namely, the out-of-phase regime is limited by a diminishing barrier on the side further away from the trap, and the in-phase drive causes a lowering of depth on the side towards the plane. For an optimal $z_0 = 1$mm trap for $^{88}\mathrm{Sr}^+$, Fig. 6 summarizes the variation in ion height, the Mathieu q-parameter, and overall trap depth as a function of ϵ under typical operating parameters. Notably, the in-phase "leakage" towards the trap surface becomes significant only when $\epsilon > 0.7$. Conservatively, this leads to a dynamic range of about $0.6z_0 = 600\mu$m that is achievable without suffering any decrease in trap depth from the single-rf configuration. Of course, a reduction in the trap depth due to this technique may be compensated by varying the magnitude of the rf voltage and the rf frequency.

Compared with previous work on shifting the rf nodal line of a four-rod linear Paul trap [30], this range is a significant increase. The underlying reason is that the geometry of the point Paul trap is more favorable for such a scheme in that a shift in the ion height does not change the symmetry of the trap axis with respect to the electrodes, in contrast to the implementation in the four-rod linear Paul trap [30] but similar to recent work on a related surface electrode ion trap [32].

The ability of the point Paul trap to vary the ion height without incurring micromotion would be of tremendous value in the search for the origin of anomalous heating in ion traps [16, 17]. Previous work on this problem have either used a technically challenging setup in which the trap electrodes were moved *in-situ* [16], or has relied on systematic testing of traps of identical geometry but different scales, making this method prone to random errors associated with the fabrication of the individual traps [17].

Anomalous heating is believed to originate from fluctuating patch potentials on the electrodes. The model describing this effect predicts a scaling of the heating rate of $1/z_0^4$; however, only one experiment has thus far been able to conduct a systematic study to confirm this [16]. As the suggested scheme for the point Paul trap in principle allows for *in-situ* variation of the ion height by almost an order of magnitude, it provides for an extremely sensitive test of the patch potential model without complications associated with physically moving the trap electrodes, and without the errors and difficulty in obtaining good statistics associated with the use of individual traps for each value of z_0.

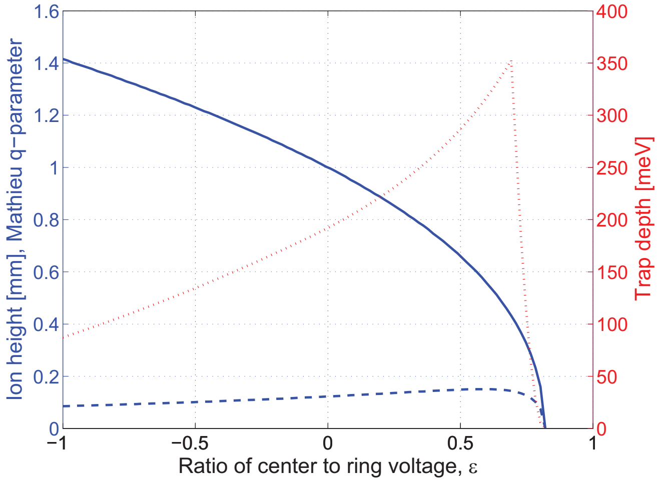

FIG. 6. (Color online) The variation in trap height (solid blue line), Mathieu q-parameter (dashed blue line) and the effective trap depth (dotted red line) as a function of the amplitude of the secondary rf. These parameters are computed for an optimal $z_0 = 1$mm (under single-rf) $^{88}\mathrm{Sr}^+$ trap, with $V_{\rm rf} = 300$V and $\Omega_{\rm rf} = 2\pi \cdot 8$MHz.

III. EXPERIMENTAL SETUP

To validate the model presented in the previous section we have tested a planar point Paul trap with an electrode geometry similar to that of section II B, and characterized its trapping of $^{88}\mathrm{Sr}^+$ ions. The trap itself is based on a printed circuit board (PCB) with copper electrodes on a low-rf-loss substrate (Rogers 4350B, fabricated by Hughes circuits)[33]. Figure 7 shows a picture of this trap mounted in a ceramic pin grid array (CPGA) chip carrier. The radius of the inner ground electrode is $a_1 = 0.550$mm, the inner radius of the rf ring electrode is $a_2 = 0.650$mm and its outer radius is $b = 3.243$mm. Due to the 100μm gap between the electrodes, the ratio $\frac{a_{1,2}}{b}$ deviates by about 10% from the optimum geometry of Table I, and produces in an ion height of $z_0 = 960\mu$m using a_2.

In this particular realization of the model system of Fig. 2, the outer ground has been segmented into four electrodes and their independent potentials can each be adjusted to compensate for stray electric fields in the vicinity of the trap. Boundary element analysis of the exact electrode configuration predicts an ion height of

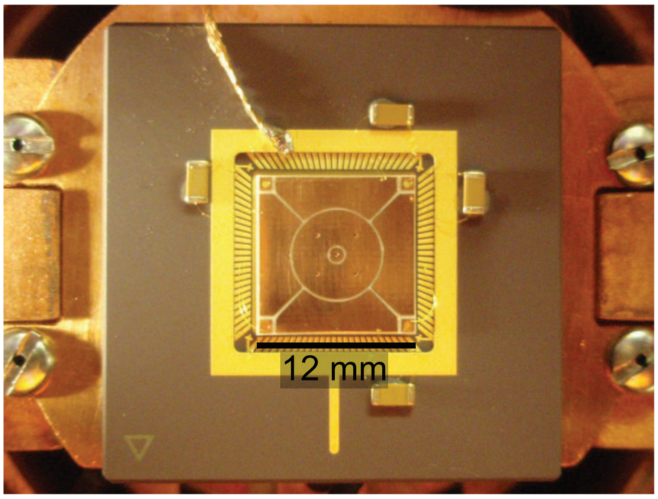

FIG. 7. (Color online) Image of the PCB trap mounted on the CPGA and installed on the 8K baseplate of the closed-cycle cryostat. Capacitors are connected to the DC electrodes in order to minimize rf pickup.

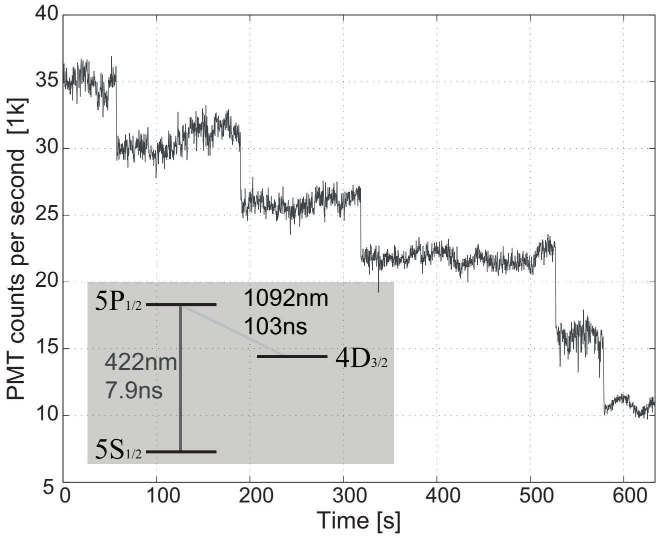

FIG. 8. Scattered 422nm light from the $5^2S_{1/2} \leftrightarrow 5^2P_{1/2}$ transition (see insert) is collected by the PMT, showing a discrete loss of five ions from the PCB trap.

940μm, in agreement with our analytical model. This analysis also finds the ratio of radial to axial secular frequencies to be $\frac{\omega_\rho}{\omega_z} \simeq 0.50$, again in good agreement with the analytic result.

The trap is mounted on the 8K baseplate of a close-cycle cryostat described in Ref. [34]. Ions are loaded via resonant photoionization of an atomic beam from an effusive oven that is heated resistively to a few hundred degrees Celcius during loading. Once ionized, the ions are Doppler-cooled using light at 422nm and 1092nm. The relevant level scheme is shown in the insert of Fig. 8 along with the lifetimes of the excited states. Typically, 20μW of 422nm light focused to a 50μm waist at the location of the ion is used for the $5^2S_{1/2} \leftrightarrow 5^2P_{1/2}$ transition, while about 20μW of 1092nm focused to a 150μm waist repumps the ion on the $4^2D_{3/2} \leftrightarrow 5^2P_{1/2}$ transition. Dark states of the $D_{3/2}$-manifold are destabilized by polarization modulation of the 1092nm light at 10 MHz as described in [35]. Fluorescence from the ions is collected with a NA$\simeq$ 0.5 lens mounted inside the vacuum chamber and imaged onto a CCD camera (Andor Luca R) and a photomultiplier tube (PMT) (Hamamatsu, H7360-02), the latter achieving an overall detection efficiency (including losses on optics in the imaging system) of 0.6%. We ensure that the ions are located at the nodal point of the rf-field by minimizing the micromotion amplitude using the correlation measurement technique as described in Ref. [29].

Radial and axial secular frequencies can be measured by applying a small sinusoidal voltage to a DC electrode, thus exciting motion along the corresponding direction [36]. At the resonant frequency of the trap, the strong increase in the amplitude of this driven motion is detected as a sudden change in the fluorescence from the ion, and can also be corroborated by increased motion along an axis by the imaging system. Depending on the trap depth, amplitude of the perturbative signal and the sweep rate, this allows a measurement of the secular frequencies with a typical accuracy of about ±5kHz.

Finally, the shift in ion height with the addition of a second rf drive is determined by the translation of the doppler cooling beam necessary in order to maximize ion fluorescence. The spatial position of the beam is calibrated by a digital translation stage with submicron resolution. However, the accuracy of this method is ultimately limited by the finite waist of the laser beams.

IV. RESULTS

The purpose of this section is to validate the model presented in Section II. Fig. 8 shows a time log of the fluorescence signal detected with the PMT as five ions are loaded and then lost from the trap. This rapid ion loss was observed prior to compensation of the stray dc fields and optimization of Doppler cooling. The discrete steps in photon counts provides a calibration of the scale to distinguish a single ion from two or more. Once compensation is optimized, we find that the trapping is stable for several hours when Doppler cooling is applied, limited only by the long-term stability of our lasers.

In addition to the discrete PMT logs, we have been able to resolve individual ions in 2D crystals involving up to nine ions, which is summarized in Figure 9. As noted in the introduction, such lattices could be used for quantum simulations of, for instance, frustrated spin systems.

The pseudopotential model for the point Paul trap is evaluated by measuring the secular frequencies of the trap for various applied rf-voltages $V_{\rm rf}$ at a constant rf-

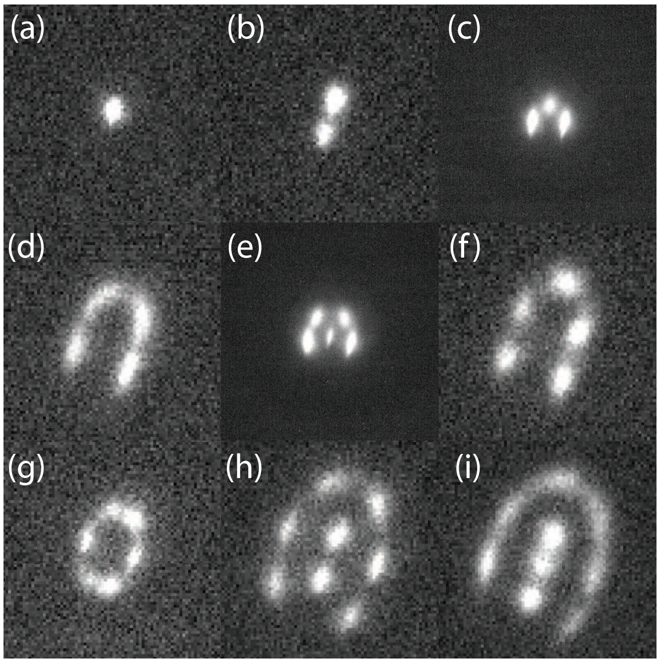

FIG. 9. Summary of the ion crystals that were observed with the PCB trap. The crystals in panels (c),(e) were observed at an ion height of 950μm ($V_{\rm rf}$ = 360V, 10s exposure) where the panel's field of view is 70μm×70μm. The remaining crystals were observed at a height of about 600μm ($V_{\rm rf}$ = 275V, $\epsilon \simeq 0.52$, 500ms exposure) where each panel corresponds to approximately 40μm×40μm.

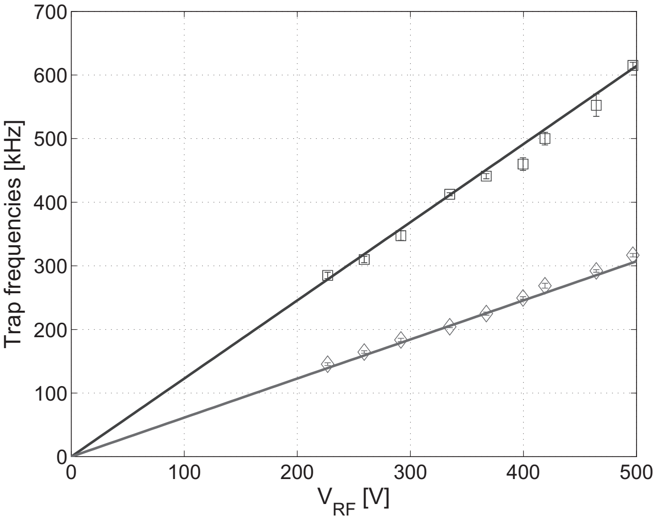

FIG. 10. Measurements of axial (square markers) and radial (diamond markers) secular frequencies of the point Paul trap. Data was taken at z_0 = 940μm under the single-rf drive at $\Omega_{\rm rf} = 2\pi \times 8.07$MHz. Also shown are theoretically expected secular frequencies (not fits) according to Eq. (14).

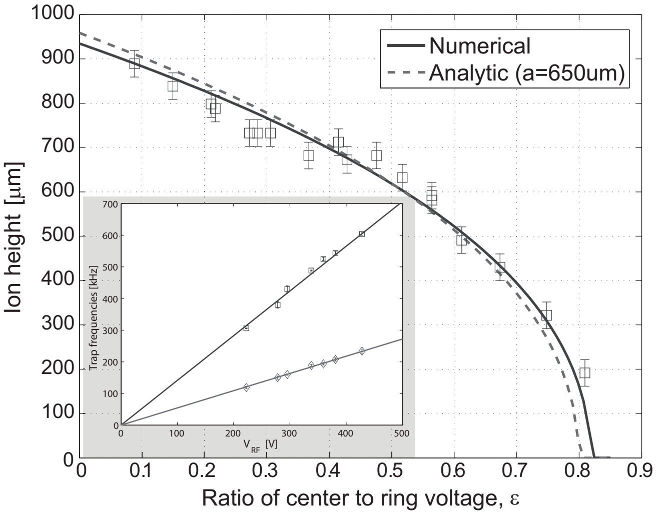

FIG. 11. Variation in ion height with the addition of the second rf on the innermost electrode. Solid curve shows the results of the numerical boundary element analysis, while the dashed curve shows the height as predicted by Eq. 25. Insert: Measured axial (squares) and radial (diamonds) trap frequencies and their fits at an ion height of 600μm.

drive frequency of $\Omega_{\rm rf} = 2\pi \times 8.07$MHz. The results are shown in Fig. 10 for a single ion held at 950μm under the single-rf scheme. Solid lines are the theoretically expected trap frequencies (not fits) according to the model of Section II. Fits through the measured data yields a ratio of the radial to axial secular frequencies of $\frac{\omega_\rho}{\omega_z} = 0.51 \pm 0.01$, in excellent agreement with the numerically predicted $\frac{\omega_\rho}{\omega_z} = 0.50$.

To establish the validity of the ion height variation model, we have explored the in-phase ($\epsilon > 0$) parameter space. The implementation of a second in-phase drive was achieved by connecting a trim capacitor between the ring and center electrodes, which then forms a capacitive divider for the center electrode in combination with the intrinsic capacitance from the PCB. Figure 11 shows the results. Experimentally, we found that stable trapping was extremely straightforward to achieve, and single ions and crystals were trapped as close as 200μm from the surface of the trap.

In addition, we were also able to measure secular frequencies when the ion was offset to a height of 600μm, as shown in the insert of Fig. 11. The comparable linearity in secular frequencies between the single- and dual-rf cases indicate that the addition of a secondary rf has not added significant micromotion to interfere with such measurements. The measured ratio of radial to axial secular frequencies was $\frac{\omega_\rho}{\omega_z} = 0.38 \pm 0.01$, which deviates significantly from the expected 0.50 (according to the model, the ratio remains unaffected by the addition of the second rf). Potential sources for deviation from the ideal model include the dc-potentials, which were added to ensure a well-compensated trap but which could have shifted secular frequencies. In particular, as the ion is brought closer to the trap surface, it is more susceptible to the effects of dc-potentials. Such fields may also break the degeneracy of the radial modes. We have in fact observed such separate radial modes, although in the case of the data in Fig. 11, they were only separated by about 20kHz, and average radial values are thus presented in that figure. We have numerically confirmed that the trap's dc potentials yield simultaneously a splitting of 20kHz in the radial modes, and a modified secular frequency ratio of 0.40.

V. CONCLUSIONS

We have presented an analytic model of a circularly-symmetric rf surface trap and its experimental validation. This particular geometry offers several advantages for further investigations in quantum information processing. Firstly, the shape of the resulting potential leads to confinement of 2D ion crystals, which may be used as a platform for lattice-based quantum simulation. Secondly, because the confinement is achieved through the ring electrode alone, the trap permits a straightforward scheme for variation of ion height *in situ*. In this work, we have demonstrated almost an order of magnitude variation of ion height, which may then, for instance, be used for a stringent test of supposed z_0^{-4} scaling in anomalous ion heating. Finally, the axial symmetry of the trap lends itself to natural integration with optical fibers. Such a device, in turn, could serve as nodes in a quantum network, or provide an interface medium between ions and cold neutral atoms.

ACKNOWLEDGMENTS

This work was supported by .... PFH is grateful for the support from The Carlsberg Foundation and the Lundbeck Foundation. THK was supported by the Siebel Scholar Foundation.

---

[1] W. Paul and H. Steinwedel, Zeitschrift Fur Naturforschung Section A-A Journal Of Physical Sciences, **8**, 448 (1953).
[2] T. Rosenband, D. B. Hume, P. O. Schmidt, C. W. Chou, A. Brusch, L. Lorini, W. H. Oskay, R. E. Drullinger, T. M. Fortier, J. E. Stalnaker, S. A. Diddams, W. C. Swann, N. R. Newbury, W. M. Itano, D. J. Wineland, and J. C. Bergquist, Science, **319**, 1808 (2008).
[3] M. A. Nielsen and I. L. Chuang, *Quantum Computation and Quantum Information* (Cambridge University Press, 2000).
[4] R. Blatt and D. Wineland, Nature, **453**, 1008 (2008).
[5] P. F. Staanum, K. Hojbjerre, P. S. Skyt, A. K. Hansen, and M. Drewsen, Nat Phys, **6**, 271 (2010).
[6] T. Schneider, B. Roth, H. Duncker, I. Ernsting, and S. Schiller, Nat Phys, **6**, 275 (2010).
[7] J. Chiaverini, R. B. Blakestad, J. Britton, J. D. Jost, C. Langer, D. Leibfried, R. Ozeri, and D. J. Wineland, Quantum Information & Computation, **5**, 419 (2005).
[8] J. Kim, S. Pau, Z. Ma, H. R. McLellan, J. V. Gates, A. Kornblit, R. E. Slusher, R. M. Jopson, I. Kang, and M. Dinu, Quantum Information & Computation, **5**, 515 (2005).
[9] D. R. Leibrandt, J. Labaziewicz, R. J. Clark, I. L. Chuang, R. J. Epstein, C. Ospelkaus, J. H. Wesenberg, J. J. Bollinger, D. Leibfried, D. J. Wineland, D. Stick, J. Sterk, C. Monroe, C. S. Pai, Y. Low, R. Frahm, and R. E. Slusher, Quantum Information & Computation, **9**, 901 (2009).
[10] S. Stahl, F. Galve, J. Alonso, S. Djekic, W. Quint, T. Valenzuela, J. Verdu, M. Vogel, and G. Werth, European Physical Journal D, **32**, 139 (2005).
[11] R. G. Brewer, R. G. DeVoe, and R. Kallnebach, Physical Review A, **46**, R6781 (1992).
[12] S. Olmschenk, D. N. Matsukevich, P. Maunz, D. Hayes, L.-M. Duan, and C. Monroe, Science, **323**, 486 (2009).
[13] L.-M. Duan and C. Monroe, Rev. Mod. Phys., **82**, 1209 (2010).
[14] R. J. Clark, T. Lin, K. R. Brown, and I. L. Chuang, Journal Of Applied Physics, **105**, 013114 (2009).
[15] K. Kim, M.-S. Chang, S. Korenblit, R. Islam, E. E. Edwards, J. Freericks, G.-D. Lin, L. Duan, and C. Monroe, Nature, **465**, 590 (2010).
[16] L. Deslauriers, S. Olmschenk, D. Stick, W. K. Hensinger, J. Sterk, and C. Monroe, Physical Review Letters, **97**, 103007 (2006).
[17] J. Labaziewicz, Y. F. Ge, P. Antohi, D. Leibrandt, K. R. Brown, and I. L. Chuang, Physical Review Letters, **100**, 013001 (2008).
[18] J. Jackson, *Classical Electrodynamics*, 3rd ed. (John Wiley & Sons, Inc., USA, 1999).
[19] M. Abramowitz and I. A. Stegun, *Handbook of Mathematical Functions With Formulas, Graphs, and Mathematical Tables* (National Bureau of Standards, 1964).
[20] H. G. Dehmelt, "Radiofrequency spectrocopy of stored ions: I storage," (Academic Press, New York, 1967) pp. 53–72.
[21] P. K. Ghosh, *Ion Traps* (Oxford University Press, New York, 1995).
[22] J. H. Wesenberg, Physical Review A, **78**, 063410 (2008).
[23] S. Seidelin, J. Chiaverini, R. Reichle, J. J. Bollinger, D. Leibfried, J. Britton, J. H. Wesenberg, R. B. Blakestad, R. J. Epstein, D. B. Hume, W. M. Itano, J. D. Jost, C. Langer, R. Ozeri, N. Shiga, and D. J. Wineland, Physical Review Letters, **96**, 253003 (2006).
[24] S. X. Wang, J. Labaziewicz, Y. Ge, R. Shewmon, and C. I. L., arXiv:0912.4892v2 (2010).
[25] M. Keller, B. Lange, K. Hayasaka, W. Lange, and H. Walther, Nature, **431**, 1075 (2004).
[26] P. F. Herskind, A. Dantan, J. P. Marler, M. Albert, and M. Drewsen, Nature Physics, **5**, 494 (2009).
[27] D. R. Leibrandt, J. Labaziewicz, V. Vuletic, and I. L. Chuang, Physical Review Letters, **103**, 103001 (2009).
[28] F. Dubin, C. Russo, H. G. Barros, A. Stute, C. Becher, P. O. Schmidt, and R. Blatt, Nat Phys, **6**, 350 (2010).
[29] D. J. Berkeland, J. D. Miller, J. C. Bergquist, W. M. Itano, and D. J. Wineland,

Journal Of Applied Physics, **83**, 5025 (1998).
[30] P. F. Herskind, A. Dantan, M. Albert, J. P. Marler, and M. Drewsen, Journal Of Physics B-Atomic Molecular And Optical Physics, **42**, 154008 (2009).
[31] M. Cetina, A. Grier, J. Campbell, I. Chuang, and V. Vuletic, Physical Review A, **76**, 041401 (2007).
[32] A. P. VanDevender, Y. Colombe, J. Amini, D. Leibfried, and D. J. Wineland, Physical Review Letters, **105**, 023001 (2010).
[33] K. R. Brown, R. J. Clark, J. Labaziewicz, P. Richerme, D. R. Leibrandt, and I. L. Chuang, Physical Review A, **75**, 015401 (2007).
[34] P. B. Antohi, D. Schuster, G. M. Akselrod, J. Labaziewicz, Y. Ge, Z. Lin, W. S. Bakr, and I. L. Chuang, Rev. Sci. Instrum., **80**, 013103 (2009).
[35] D. J. Berkeland and M. G. Boshier, Physical Review A, **65**, 033413 (2002).
[36] H. Naegerl, R. Blatt, J. Eschner, F. Schmidt-Kaler, and D. Leibfried, Opt. Express, **3**, 89 (1998).